RSC Advances

PAPER

View Article Online
View Journal | View Issue

Cite this: *RSC Adv.*, 2025, **15**, 9141

Fabrication of anti-fouling and self-cleaning PHI modified PVDF membranes for high-flux dye removal†

Liwen Xiao,[a] Long Chen,*[a] Huijun Xu,[b] Ziyu Huang,[a] Zhixuan Wang,[a] Fang Liu,[a] Wenbin Wang[c] and Qingyang Du*[a]

The large pore size of ultrafiltration membranes presents a challenge in rejecting small molecules and the accumulated contaminants on the membrane surface severely restrict the treatment efficiency and shorten the lifespan of separation membranes. Herein, poly(heptazine imide) (PHI) is utilized as a modifier to fabricate anti-fouling and self-cleaning polyvinylidene fluoride (PVDF) membranes for high-flux dye removal. The introduction of PHI does not affect the rejection performance of bovine serum albumin (>97%), whilst improving the water permeability and mechanical strength of membranes. The anti-fouling ability is also significantly enhanced with a flux recovery ratio of 91.61%. In addition, the rejection performance of PHI modified PVDF (PHI/PVDF) membranes for anionic dyes, especially for those of low molecular weight, is obviously improved. The rejection ratios of Congo red (CR) and orange G are 99.8% and 87.4%, respectively, and rejection performance for methyl orange is increased from 22.0% (pure PVDF membrane) to 62.5% (M3 membrane with 3 g PHI added). Furthermore, in the presence of anionic dye (such as CR), 99.3% of methylene blue, 91.8% of malachite green and 95.9% of basic red 46 can be rejected and approximately 613 L m^{-2} of 50 mg per L CR solution can be processed after 2 h of operation, with the rejection ratio consistently above 98%. The accumulated CR dyes on PHI/PVDF membranes can be easily self-cleaned within 60 min by the H_2O_2-assisted photocatalytic reaction, effectively solving the problem of membrane fouling.

Received 12th January 2025
Accepted 15th March 2025

DOI: 10.1039/d5ra00279f

rsc.li/rsc-advances

1 Introduction

The advantages of simple operation, high efficiency and low energy consumption have led to the widespread use of membrane separation technology in the fields of water treatment, industrial production, energy conversion, environmental protection, *etc.*[1–4] Ultrafiltration membranes, as a class of separation membrane materials, have the superiority of easy synthesis by the non-solvent induced phase separation (NIPS) method[5,6] and easily adjustable membrane structure by regulating the synthesis parameters.[7,8] Because of the pore size of 0.01–0.1 μm, ultrafiltration membranes can effectively reject macromolecules, such as proteins, bacteria, polysaccharides, *etc.* Therefore, bovine serum albumin (BSA, 66 kDa) is usually chosen as the typical model system to evaluate the separation performance.[9–11] However, the large pore size of ultrafiltration membranes makes it difficult to reject low molecular weight dyes (<1 kDa).[12,13] As a result, the applications are severely limited. To expand the application of ultrafiltration membranes to dyeing wastewater, the current research mainly focuses on the adsorption effect.[14,15] Nevertheless, the adsorption method suffers from the problems of adsorption saturation and low efficiency, which limits the long-term application of ultrafiltration membranes.[16]

Electrostatic repulsion is an effective means of achieving efficient separation for dyes. Hu *et al.*[17] prepared PES/SPSf tight ultrafiltration membrane with the rejection performance for methyl orange, acid blue 25, Evans blue of 69.4%, 92.6%, 100%, respectively. The high rejection ratio of dyes was attributed to the synergistic effect of molecular sieve and electrostatic repulsion. Moghadam *et al.*[18] prepared 1 wt% GO-PVA-NaAlg/PVDF ultrafiltration membrane. The rejection ratio of methyl orange and Congo red was 93.6% and 95.9%, respectively, which was mainly due to the electrostatic repulsion between the dye molecular and membrane surface. Although electrostatic repulsion can improve the dye rejection performance of ultrafiltration membranes, it is only capable of effectively rejecting dyes with the same charge, and is unable to reject dyes with opposite charges. Furthermore, dye molecules inevitably

[a]School of Materials Science and Engineering, Shandong University of Technology, Zibo 255049, China. E-mail: lchen830@sdut.edu.cn; qydu@sdut.edu.cn
[b]School of Chemistry and Chemical Engineering, Shandong University of Technology, Zibo, Shandong 255049, China
[c]College of Materials Science and Engineering, Xi'an University of Science and Technology, Xi'an 710054, China

† Electronic supplementary information (ESI) available. See DOI: https://doi.org/10.1039/d5ra00279f

accumulate on the membrane surface, decreasing the treatment efficiency and lifespan of ultrafiltration membranes. Therefore, efficient removal of dye molecules deposited on membranes is of great importance for practical water treatment applications.

Physical cleaning (water rinsing) and chemical cleaning (acid and base cleaning) are the most commonly used methods for alleviate the organic fouling on membranes. However, they can cause the irreversible damage to the membrane structure, as well as the waste of clean water and secondary water pollution. The modification of membranes is an attractive strategy to solve the problem of membrane fouling, including the surface modification (grafting,[19] coating,[20] self-assembly[21]) and blending modification (polymers[22] and inorganic nanoparticles[23]). Nevertheless, these strategies are still inevitably succumbed the deposition of dye molecules on membranes during the separation operation.

The coupling of catalytic technology with membrane separation to decompose organic foulants is undoubtedly more effective than preventing their deposition on membranes. For example, Zhang *et al.*[23] constructed Ag@BiOBr/PVDF photocatalytic membrane reactor with excellent anti-fouling ability. The BSA foulant blocked in membrane pores and accumulated on membrane surface could be easily removed under visible light irradiation. Wei *et al.*[24] reported that the modification of polydopamine and $FeVO_4$ on PVDF membrane endowed it with superior anti-fouling property. The flux recovery rate could be maintained at a high level of 92.5% after 3 cycles, which was significantly improved compared to the pristine PVDF membrane (72.5%). However, the incorporation of these anti-fouling agents mainly endows the separation membranes with anti-fouling ability, but fails to effectively reject small molecular dyes. Additionally, most of anti-fouling agents are inorganic materials, which raises the issue of compatibility with the polymeric PVDF matrix. Therefore, it is of great importance to screen an anti-fouling agent that is compatible with the PVDF membrane matrix to solve membrane fouling while endowing the membrane with effective rejection ability for dyes to extend its application range.

Poly(heptazine imide) (PHI) is a two-dimensional layered polymeric material composed of heptazine ring (tri-*s*-triazine ring) units (Fig. S1(a)†).[25] The abundant terminal imino groups (–NH) in PHI can form hydrogen bonds with $-CF_2$ groups in PVDF. Therefore, the binding force between PHI and PVDF is significantly enhanced.[26] The enhanced interaction between PHI and PVDF as well as the polymeric nature of PHI can effectively mitigate the compatibility issue compared to other inorganic anti-fouling agents. In addition, PHI is an excellent visible light responsive semiconductor photocatalyst, with the advantages of facile synthesis, controllable structure, environmental compatibility, and remarkable resistance to both strong acidic and alkaline conditions.[27] Therefore, PHI is a potential anti-fouling agent for polymeric membranes to resolve the organic fouling. Furthermore, the negatively charged PHI can increase the charge amount on the membrane surface, thereby enhancing the electrostatic repulsion ability to anionic dyes.[28] However, to the best of our knowledge, there is little relevant research on using PHI as the anti-fouling agent to fabricate highly efficient self-cleaning membranes for high-flux dye removal.

Herein, polyvinylidene fluoride (PVDF) was used as a representative membrane matrix. A series of PHI modified PVDF (PHI/PVDF) membranes were prepared *via* the NIPS method by regulating the PHI additions. The effects of PHI addition on crystalline structure, morphology, pore structure, mechanical property, hydrophilicity and water permeability of PHI/PVDF membranes were systematically investigated. In addition, BSA and different dyes were separately chosen as the model system to evaluate the separation performance. And anti-fouling ability and self-cleaning performance were further studied. The mechanism of dye rejection and self-cleaning ability was also proposed based on a series of experimental results. This work provided a feasible approach for the fabrication of efficient anti-fouling and self-cleaning membranes for protein separation and high-flux dye removal.

2 Experimental section

2.1. Chemicals and reagents

Polyvinylidene fluoride (PVDF, Solef®6010) was purchased from Solvay Co., Ltd. *N*,*N*-Dimethylformamide (DMF, ≥99.5%), polyvinyl pyrrolidone (PVP, K30, GR), triethanolamine (TEOA, ≥78.0%) and rhodamine B (RhB, AR) were obtained from Sinopharm Group Chemical Reagents Co., Ltd. Potassium chloride (KCl, ≥99.5%), potassium bromate ($KBrO_3$, 99.8%), orange G (OG, BS) and basic red 46 (BR46, Strength: 250%) were bought from Shanghai Macklin Biochemical Technology Co., Ltd. Melamine (99.0%) and humic acid (HA, 90%) were come from Shanghai Titan Technology Co., Ltd. Hydrogen peroxide (H_2O_2, 30%) was acquired from Yantai Shuangshuang Chemical Co., Ltd. Bovine serum albumin (BSA, 68 kDa, 96.0%) was get from Shanghai Aladdin Biochemical Technology Co., Ltd. Methanol (MeOH, ≥99.5%) was obtained from Shanghai Tianlang Technology Co., Ltd. Chloroform (CF, ≥99.0%), methyl orange (MO, AR) and malachite green (MG, AR) were purchased from Tianjin Bondi Chemical Co., Ltd. Methylene blue (MB, ≥98.5%) was bought from Tianjin Zhiyuan Chemical Reagent Co., Ltd. Congo red (CR, IND) was acquired from Tianjin Komio Chemical Reagent Co., Ltd. All chemical reagents were directly used without further purification. Deionized water was used throughout the experiment.

2.2. Sample preparation

2.2.1. Preparation of PHI catalyst. PHI was synthesized by the thermal polycondensation method assisted with KCl as molten salt.[29] Melamine was used as raw material. Typically, 1 g of melamine and 6 g of KCl were thoroughly ground. The obtained mixture was transferred into a crucible and sealed with aluminum foil, and then heated at 600 °C for 2 h with the heating rate of 5 °C min^{-1}. The calcined products were ground, washed with deionized water, dried at 60 °C for 6 h. And thus, bright yellow PHI samples were obtained (Fig. S1(b)†).

2.2.2. Fabrication of PHI modified PVDF membranes. PHI modified PVDF membranes were prepared by the NIPS method.

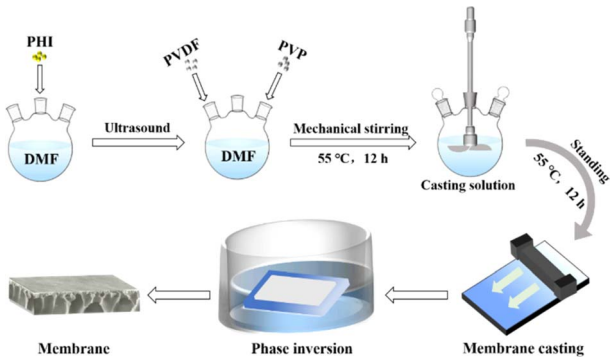

Fig. 1 Synthetic diagram of PHI/PVDF membranes.

The preparation process was shown in Fig. 1. Firstly, a certain amount of PHI powder was dispersed into 83.3 mL of DMF solution with ultrasonic for 30 min to obtain a uniform suspension. Then, 3 g of PVP and 18 g of PVDF powder were added and stirred at 55 °C for 12 h to obtain the casting solution. The casting solution was stood at 55 °C for 12 h to eliminate bubbles, and then poured onto a clean glass plate, scraped with a 100 μm scraper. The obtained liquid film was stood in air for 15 s, and placed into deionized water for phase inversion. After 24 h for the complete phase inversion, PHI/PVDF membranes were prepared. According to the adding amount of PHI powder (0 g, 0.5 g, 1 g, 2 g, 3 g), the prepared PHI/PVDF membranes were named as M0, M0.5, M1, M2 and M3, respectively.

2.3. Characterizations

Phase structure, surface functional groups and morphology of PHI catalyst were analyzed by X-ray diffraction (XRD, D8 Advance), Fourier transform infrared spectroscopy (FTIR, Nicolet 5700) and transmission electron microscope (TEM, G2F 20), respectively. Surface and cross-sectional morphology and pore structure of PHI/PVDF membranes were observed by scanning electron microscopy (SEM, Apreos). The pore size of sponge-like pores in the inner pore wall was measured by the software of Nano Measurer. After measuring the pore sizes by randomly selecting 100 pores, the pore size distribution was statistically calculated. The distribution of PHI in the membrane was analysed by energy dispersive spectroscopy (EDS, Apreos). Surface charge property of PHI and PHI/PVDF membranes was determined by micro-electrophoresis instrument (JS94) and solid-surface zeta potential instrument (Surpass 3), respectively. Water contact angle was measured by video contact angle tester (SDC-200S) to characterize the surface hydrophilicity, which was measured three times to ensure the accuracy. Mechanical property was evaluated by tensile breaking strength and elongation at break, and tested on an electronic tensile tester (DR-6010A). Each membrane was measured five times. The overall porosity (ε) of the membrane was measured three times by the gravimetric method, and calculated by the following formula.

$$\varepsilon(\%) = \frac{M_w - M_d}{\rho V} \quad (1)$$

where ε was the overall porosity of the membrane, M_w was the weight of wet membrane, M_d was the weight of dry membrane, ρ was the density of pure water (1 g cm^{-3}), V was the volume of the membrane (cm^3).

2.4. Performance test

2.4.1. Water permeability. Water flux was measured by a self-made membrane performance tester in the cross-flow mode (both valves 1 and 2 open) to evaluate the water permeability of the membrane (Fig. S2†). A diaphragm pump (DP-60A-24V) was used as the pressure driver. The tested membrane was put into a membrane pool and pre-pressed at 1.2 bar by deionized water to obtain the stable water flux. After that, the permeate volume of different solution (pure water, BSA solution and dye solution) was collected and recorded as V. Each membrane was tested three times and the average value was taken as the final result. The water flux was calculated by the following formula.

$$\text{Water flux} = \frac{V}{AtP} \quad (2)$$

where A was the effective area of the membrane (7.5×10^{-4} m^2), t was the testing duration (h), and P was operating pressure (bar).

2.4.2. Ultrafiltration performance. The ultrafiltration performance of prepared membranes was evaluated by the rejection of BSA and different dyes, separately, which was also measured by the self-made membrane performance tester in the cross-flow mode (Fig. S2†). Typically, the membrane was also pre-pressed at 1.2 bar by deionized water. And then, the feed solution was replaced by BSA solution (1 g L^{-1}) or different dyes solution (50 mg L^{-1}). The feed and permeate BSA or dyes solution were taken and measured by a UV-vis spectrophotometer (UV-2450) to obtain the feed concentration (C_p) and permeate concentration (C_f). The rejection ratio of BSA (BRR) and different dyes was calculated by eqn (3).

$$\text{Rejection ratio}(\%) = 1 - \frac{C_p}{C_f} \quad (3)$$

For the dye rejection, different anionic and cationic dyes with different molecular weight were selected, including malachite green (MG), methylene blue (MB), basic red 46 (BR46), rhodamine B (RhB), methyl orange (MO), orange G (OG), Congo red (CR). The basic information of these dyes was given in Table S1.† In addition, the rejection performance for different mixed dyes was also tested by mixing different cationic dyes (50 mg L^{-1}) with anionic dyes (50 mg L^{-1}). The rejection stability and treatment efficiency of M1 and M0 membranes for CR solution was evaluated for 2 h. The operating pressure for dye rejection was kept at 1.2 bar.

2.4.3. Anti-fouling performance. Anti-fouling performance of the membranes was evaluated by the flux recovery ratio (FRR). After the membrane was pre-pressed at 1.2 bar by deionized water, the flux of pure water was recorded as J_1. And the flux of BSA solution (1 g L^{-1}) or HA solution (0.5 g L^{-1}) was marked as J_2. Then, the used membrane for the rejection of BSA

or HA was ultrasonically treated and further used to retest the pure water flux (J_3). The procedure was repeated twice. To assess the effect of ultrasonic treatment on the membrane structure, the rejection ratio of BSA and HA was measured after ultrasonic treatment. The FRR, reversible fouling resistance (R_r), irreversible fouling resistance (R_{ir}) and total fouling resistance (R_t) were obtained by the following equations.

$$\mathrm{FRR}(\%) = \frac{J_3}{J_1} \quad (4)$$

$$R_r(\%) = \frac{J_3 - J_2}{J_1} \quad (5)$$

$$R_{ir}(\%) = \frac{J_1 - J_3}{J_1} \quad (6)$$

$$R_t(\%) = \frac{J_1 - J_2}{J_1} \quad (7)$$

2.4.4. Self-cleaning performance. The self-cleaning performance was evaluated by the H_2O_2-assisted photocatalytic reaction. The polluted membranes by dyes were put into a beaker containing 1 mL of H_2O_2 solution (30%) and 100 mL of deionized water. The beaker was positioned at a distance of 20 cm from the Xenon lamp (350 W). And then, Xenon lamp was turned on to start the catalytic reaction. The color changes of the polluted membranes were recorded at different reaction time. For comparison, the self-cleaning performance was also evaluated under the same conditions in the absence of H_2O_2 or light.

2.4.5. Trapping experiments for free radicals. To explore the generated reactive species involved in PHI/H_2O_2/light catalytic system, CR was used as the target organic pollutant. Methanol (MeOH), chloroform (CF), triethanolamine (TEOA) and $KBrO_3$ were used as the scavenger of hydroxyl radical ($^{\bullet}OH$), superoxide radical ($^{\bullet}O_2^-$), photogenerated holes (h^+) and electrons (e^-), respectively. Typically, 0.1 g of PHI catalyst was dispersed into 100 mL of CR solution (20 mg L^{-1}) in the presence of a certain scavenger. After stirring for 30 min in dark to achieve the adsorption–desorption equilibrium, H_2O_2 (80 mmol L^{-1}) and light (350 W Xenon lamp) was introduced to start the catalytic reaction. 4 mL of suspension was taken every 10 min and filtered by 0.22 μm filter membrane. The obtained filtrate was measured by a UV-vis spectrophotometer (UV-2450). The residual concentration of CR solution was calculated according to the Lambert–Beer's law. Based on the degradation efficiency of CR, the role of different reactive species was determined in the catalytic reaction.

3 Results and discussion

3.1. Characterization of physicochemical properties

Phase structure of PHI sample is analysed by XRD. As shown in Fig. 2(a), the characteristic (100) crystal plane at 8.0° is detected, which reflects the in-plane repeating units of PHI framework, indicating the successful preparation of PHI.[29,30] In addition, the peak at 28.2° is ascribed to the (002) crystal plane,

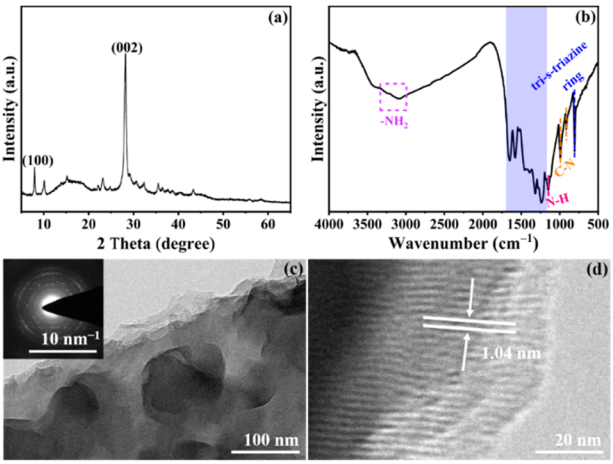

Fig. 2 (a) XRD pattern, (b) FTIR spectrum, (c) TEM image and SAED pattern (inset), (d) HRTEM image of PHI.

representing the interlayer stacking of conjugated aromatic system.[31] FTIR is further used to determine the functional groups in PHI. As shown in Fig. 2(b), the peaks at 802 cm^{-1} and 1200–1700 cm^{-1} (blue region) are belonged to the out-of-plane bending vibration and stretching vibration of the tri-*s*-triazine ring in PHI, respectively.[29,32] The peaks at 914 cm^{-1} and 995 cm^{-1} are assigned to the characteristic vibration of C–N bond in the tri-*s*-triazine ring. And the peaks at 1153 cm^{-1} and 3000–3400 cm^{-1} are corresponded to the N–H bending vibration and terminal amino group (–NH_2), respectively. The presence of abundant –NH/–NH_2 groups can form hydrogen bonds with water molecules, and thus making PHI to be a hydrophilic material.[30,33] TEM image in Fig. 2(c) shows that the PHI sample exhibits the typical lamellar structure. SAED proves the polycrystalline structure of PHI.[34] The lattice fringe of 1.04 nm in the HRTEM image (Fig. 2(d)) corresponds to the (100) crystal plane of PHI,[35] further verifying the successful preparation of crystalline PHI.

Fig. 3(a) shows the XRD patterns of pure PVDF and PHI/PVDF membranes. The characteristic diffraction peak at 20.6° is attributed to the (200) crystal plane of β phase in PVDF.[36] While the small shoulder peak at around 18.6° is ascribed to the (020) crystal plane of α phase in PVDF.[37] Upon the introduction of PHI, the characteristic diffraction peak of PHI (002) crystal plane is detected at 28.2°. The peak intensity is gradually

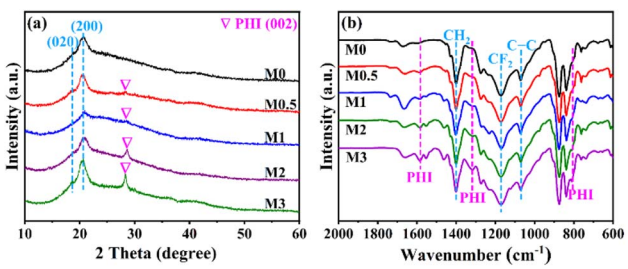

Fig. 3 (a) XRD patterns and (b) FTIR spectra of pure PVDF and PHI/PVDF membranes.

enhanced with the increase in PHI amount. This result indicates that PHI is successfully mixed into the PVDF matrix. The FTIR spectra of pure PVDF and PHI/PVDF membranes are shown in Fig. 3(b). In the case of the pure PVDF membrane, the peak at 1400 cm^{-1} is belonged to the bending vibration peak of $-CH_2$. The peaks at 1182 cm^{-1} and 1072 cm^{-1} are assigned to the tensile vibration peaks of $-CF_2$ and C–C in PVDF, respectively.[26] These peaks are all detected in the PHI/PVDF membranes. In addition, obvious new peaks at 802 cm^{-1}, 1320 cm^{-1} and 1580 cm^{-1} are appeared, which are belonged to the vibration of tri-*s*-triazine ring in PHI. And the peak intensities gradually increase with the PHI additions. This result further proves that PHI has been successfully mixed into PVDF matrix.

Surface and cross-sectional morphology and pore structure are observed by SEM. It can be seen from Fig. 4(A-a) that a small number of pores are present on the top surface of pure PVDF membrane. However, once PHI is introduced (M0.5 and M1), the size of pores on the top surface is obviously reduced and can't be observed (Fig. 4(B-a and C-a)). This may be due to the strong interaction (hydrogen bond) between PHI and PVDF,[38–41] making the PVDF molecular chains be more closely intertwined, thus forming a network pore with a smaller pore size. This is further evidenced by the sponge-like pores formed on the inner wall of membranes (Fig. 4(c)). From the size distributions of sponge-like pores on the inner wall of membranes, it can be seen that the mean pore size basically reduces with increasing PHI addition, which obviously decreases when the amount of PHI is more than 1 g (Fig. 4(d–h)). The increased PHI content enhances the interfacial interactions with PVDF, promoting entanglement of PVDF molecular chains and consequently reducing the size of sponge-like pores. Nevertheless, the size of pores on the top surface of M2 and M3 membranes is significantly increased (Fig. 4(d-a and E-a)). And the number of the pores on M3 membrane is more than M2 membrane. The reason for the increased surface pores on M2 and M3 membranes can be ascribed to the inevitable aggregation of PHI in membranes when the PHI addition is high (Fig. 4(D-c and E-c)).[42] The hydrophilic aggregated PHI on the top surface enhances the interaction with non-solvent,[43–45] thus repelling PVDF molecules and forming the polymer-lean phase, which eventually transforms into larger surface pores (M2 membrane). As the PHI addition is further increased (M3 membrane), the PHI aggregates more seriously. And the interaction between PHI and non-solvent becomes more apparent. As a result, the size and amount of surface pores on M3 membrane continue to increase. While PHI disperses uniformly at low concentration (M0.5 and M1 membrane) with much smaller particle size. Therefore, this effect is not obvious. The cross-sectional morphology in Fig. 4(A-b) shows that the pure PVDF membrane exhibits the typical asymmetric structure, which is mainly composed of surface skin-layer and inner pear-like pores. The formation of pear-like pores is due to the exchange process between solvents and non-solvents.[46] The introduction

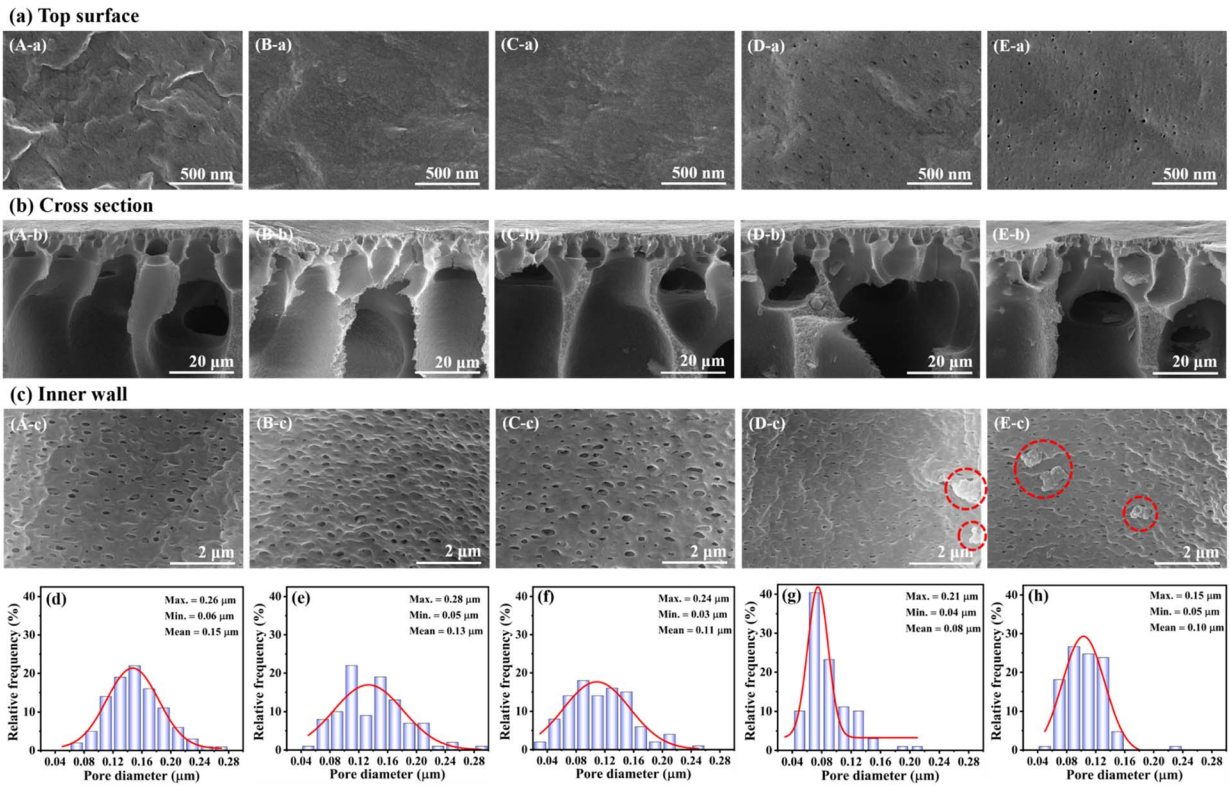

Fig. 4 SEM images of pure PVDF and PHI/PVDF membranes: (a) top surface, (b) cross section, (c) inner wall (A – M0, B – M0.5, C – M1, D – M2, E – M3), and pore size distributions of sponge-like pores on the inner wall of (d) M0, (e) M0.5, (f) M1, (g) M2 and (h) M3 (note: the region marked by the red line is the PHI agglomerates).

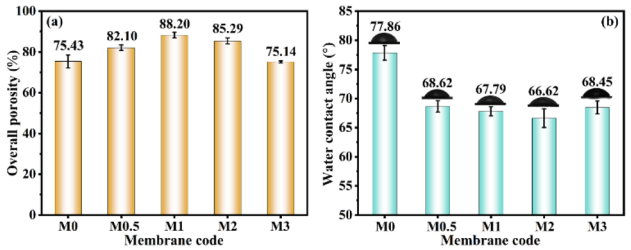

Fig. 5 (a) The overall porosity and (b) water contact angle of pure PVDF and PHI/PVDF membranes.

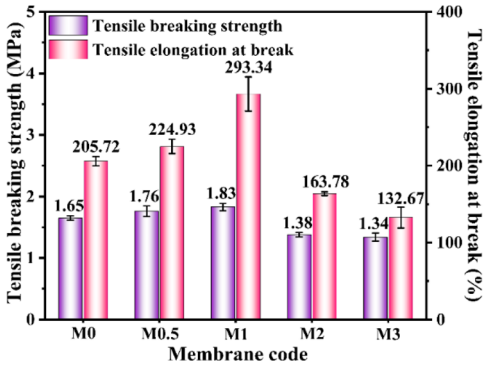

Fig. 6 Tensile breaking strength and elongation at break of pure PVDF and PHI/PVDF membranes.

of PHI doesn't obviously change the inner pore structure of membranes. From the EDS mapping images in Fig. S3,† N element is uniformly distributed, indicating that PHI is successfully and uniformly blended into the PVDF matrix.

The overall porosity of prepared membranes is measured by the gravimetric method. The result is given in Fig. 5(a). It can be seen that the overall porosity of PHI/PVDF membranes increases and then decreases with the increase in the PHI amount. The introduction of moderate amount PHI is beneficial for the increase in overall porosity. This may be attributed to the hydrophilicity of PHI, enhancing the interaction with non-solvent, and thus forming large amounts of small pores (polymer-lean phase) in membranes.[44,45,47] However, once the adding amount of PHI exceeds 1 g, the overall porosity of PHI/PVDF membranes (M2 and M3) decreases, which can be ascribed to the blocking effect of PHI aggregates. This is consistent with the SEM results (Fig. 4(D-c and E-c)). Subsequently, the effect of PHI on the hydrophilicity of membranes is investigated by the water contact angle. As shown in Fig. 5(b) and S4,† the water contact angle of pure PVDF membrane is 77.86°. After 3 min of contact, the contact angle is slightly reduced to 71.12°. This result implies that pure PVDF membrane is intrinsic hydrophobicity.[48] After the introduction of PHI, the water contact angle of PHI/PVDF membranes is significantly reduced and decreases with the extension of contact time. The improved hydrophilicity is due to the presence of hydrophilic PHI on the membrane surface, which is migrated to the membrane/water interface during the phase conversion process.[49,50] The abundant hydrophilic functional groups (–NH/–NH_2) in PHI enhances the interaction with water molecules and thus facilitates water transport across the membrane.[45,51,52]

Mechanical strength is of great significance in ensuring the stability of the membrane during separation operation. Therefore, it is necessary to evaluate the impact of PHI on mechanical property. As shown in Fig. 6 and S5,† the introduction of a certain amount of PHI leads to the increase in the tensile breaking strength and elongation at break (M0.5 and M1). When the PHI addition is 1 g, the tensile breaking strength and elongation at break is increased from 1.65 MPa and 205.72% of M0 membrane to 1.83 MPa and 293.34% of M1 membrane, respectively. And the mechanical strength of M1 membrane is superior to other modified PVDF membranes (Table S2†). The enhanced mechanical property can be attributed to the fact that PHI nanosheets can act as cross-linking nodes to connect PVDF chains, and thus enhancing the mechanical strength.[44,53,54] In addition, the abundant –NH groups in PHI can form hydrogen bonds with –CF_2 groups in PVDF. The formed hydrogen bonds can significantly enhance the binding force between PHI and PVDF, thereby making the PVDF chains to be not easy to be broken during stretching.[26,39,55] However, once PHI is added more than 1 g, the tensile breaking strength and elongation at break of M2 and M3 membranes are significantly reduced, which is generally ascribed to the partial agglomeration of PHI (Fig. 4(D-c and E-c)).[53,56,57]

3.2. Evaluation of membrane performance

3.2.1. Water permeability. The water flux of prepared membranes is measured to assess the water permeability. As shown in Fig. 7, the introduction of PHI significantly improves the pure water flux. When PHI addition is 1 g, the pure water flux of M1 membrane increases from 255.24 L m^{-2} h^{-1} bar^{-1} (pure PVDF membrane) to 361.31 L m^{-2} h^{-1} bar^{-1}, which is improved by 41.6%. The enhanced water permeability can be attributed to the improved hydrophilicity and increased porosity (Fig. 5). Nevertheless, once the adding amount of PHI is more than 1 g, the pure water flux of M2 and M3 membranes increases slightly. This may be ascribed to the result of mutual cancellation of increased pore size of upper surface and decreased porosity (Fig. 4(D-a, E-a) and Fig. 5). In addition,

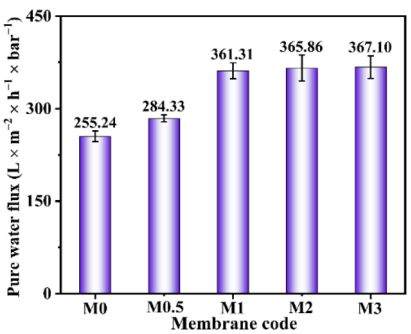

Fig. 7 The pure water flux of pure PVDF and PHI/PVDF membranes.

similar trends have also been obtained in the BSA flux (Fig. S6†) and CR flux (Fig. S7†). The significantly reduced BSA flux is ascribed to the blockage of BSA on the membrane pores.

3.2.2. BSA rejection and anti-fouling performance. Firstly, the BSA rejection ratio (BRR) is used to evaluate the ultrafiltration performance of pure PVDF and PHI/PVDF membranes. As shown in Fig. 8(a), the introduction of PHI doesn't affect the BSA rejection performance. The BRR values are even slightly increased in the PHI modified PVDF membranes (above 97%). The enhanced BSA rejection performance can be due to the formed water layer induced by the hydrophilic PHI, which hinders the adsorption/contact of BSA onto membrane.[51,53,58] What's more, the introduction of PHI significantly enhances the anti-fouling performance. The flux recovery ratios (FRR) of M0.5 and M1 membranes reach 91.61% and 89.97%, respectively, which are much higher than 72.06% of pure PVDF membrane. In addition, the reversible fouling resistance (R_r) of M0.5 and M1 membranes increases evidently, along with the dramatically reduced irreversible fouling resistance (R_{ir}) (Fig. 8(b)). This result indicates that BSA molecules attached to M0.5 and M1 membranes are more easily removed. The reason may be attributed to the enhanced hydrophilicity. The formed water layer on M0.5 and M1 membranes can reduce the adhesion of BSA molecules on the membrane surface, which cause the BSA molecules to be easily removed under ultrasound. As evidenced by the SEM images in Fig. S8(d and f),† the surface of M1 membrane is clean after ultrasonic treatment. Almost all BSA molecules have been removed from M1 membrane. However, massive BSA molecules still remain on the surface of M0 membrane (Fig. S8(c and e)†). This can be ascribed to the strong hydrophobicity of M0 membrane, which has strong interaction with BSA molecules, making it difficult to remove the deposited BSA molecules under ultrasound. In addition, once the adding amount of PHI exceeds 1 g, the anti-fouling performance is remarkably down. This is because the pore sizes on the top surface of M2 and M3 membranes are much larger (Fig. 4(D-a and E-a)), due to the aggregation of PHI. BSA molecules easily enter the interior of the membranes and thus difficult to be removed.

To comprehensively validate antifouling capabilities of PHI/PVDF membranes, the time-dependent flux and rejection ratio of different foulants (BSA and HA) are investigated in three stages. As shown in Fig. 9(a and b), the rejection rates of BSA and HA show only a slight decrease after two cycles of ultrasonic treatment, but can still be maintained above 94.5% and 93.4%,

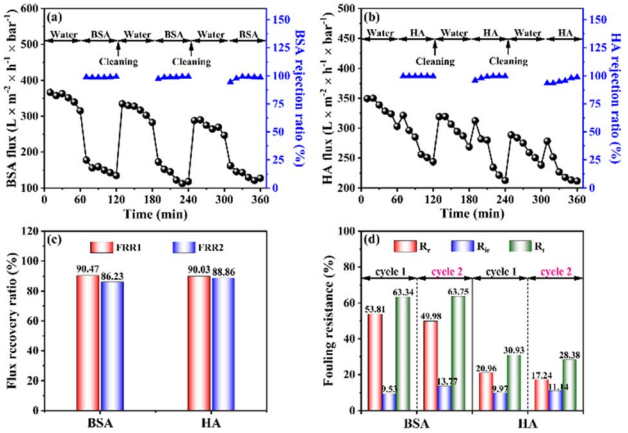

Fig. 9 Time-dependant flux and rejection ratio of (a) BSA and (b) HA, (c) flux recovery rate and (d) fouling resistance of BSA and HA by M1 membrane under two cycles.

respectively. After the first cycle, the flux recovery rates of BSA and HA are 90.47% and 90.03%, respectively. And the flux recovery rates only decrease to 86.23% and 88.86% after the second cycle, demonstrating the excellent anti-fouling performance of the M1 membrane (Fig. 9(c)). The reason for the excellent anti-fouling capacity is that the reversible fouling resistance dominates and most of the organic foulant can be effectively removed by ultrasound. The decrease in the second flux recovery rate is due to the presence of irreversible fouling resistance, which prevents the effective removal of organic foulant deposited in the membrane pores and leads to the decrease in flux. In addition, it can be seen from Fig. 9(d) that the total fouling resistance of HA is much lower, indicating that the membrane surface is not easily adhered or blocked by HA. Therefore, the flux of HA solution is significantly higher than that of BSA, due to the hydrophilicity of HA.

3.2.3. Dye rejection performance. To evaluate the effect of PHI modification on ultrafiltration performance of prepared membranes for small molecules, various anionic and cationic dyes with different molecular weight are chosen as the model system. As shown in Fig. 10, the rejection ratio of M0 membrane for different dyes generally increases with the molecular weight (99.3% of CR (696.6 g mol^{-1}) > 87.9% OG (452.3 g mol^{-1}) >

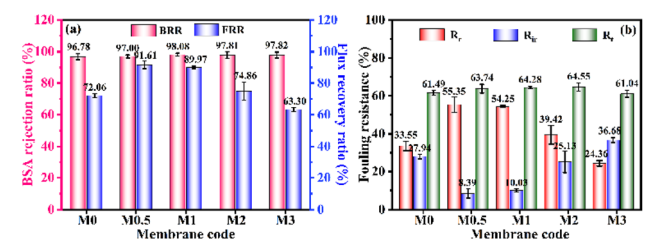

Fig. 8 (a) BSA rejection ratio and water flux recovery ratio, and (b) fouling resistance of pure PVDF and PHI/PVDF membranes.

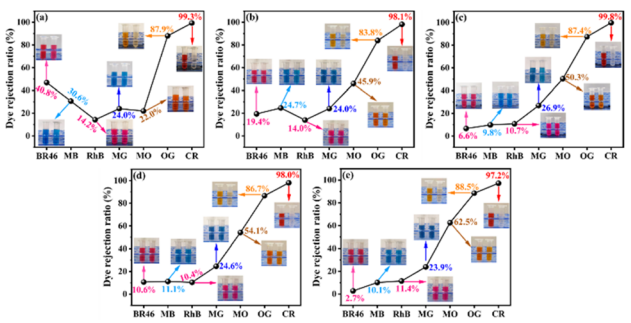

Fig. 10 Comparison of the rejection performances of (a) M0, (b) M0.5, (c) M1, (d) M2, and (e) M3 membranes for different dyes.

40.8% BR46 (401.31 g mol^{-1}) > 30.6% of MB (373.9 g mol^{-1}) > 24.0% of MG (364.92 g mol^{-1}) > 22.0% of MO (327.3 g mol^{-1})) (Fig. 10(a)). Therefore, the molecular sieving effect plays the crucial role in the rejection of dyes for M0 membrane. While the surface charge on M0 membrane has little effect, due to the small Zeta potential of −8.56 mV (Fig. S9†). The exception of RhB (14.2%, 479.01 g mol^{-1}) may be ascribed to the presence of carboxylic group (–COOH). The deprotonation of –COOH makes RhB transform into a zwitterionic structure,[59] which has the better wettability for PVDF membrane and thus is easier to penetrate the membrane pore. Compared with the M0 membrane, the rejection performances of PHI/PVDF membranes for cationic dyes and anionic dyes are significant different. The reason can be mainly ascribed to the increased negative charges in the PHI/PVDF membranes, which increases with increasing the PHI addition (Fig. S9†). The increased negative charge of PHI/PVDF membranes is attributed to the introduction of negatively charged PHI, which possesses the Zeta potential of −40.11 mV. For cationic dyes, the rejection performances of PHI/PVDF membranes for BR46 and MB are reduced (Fig. 10). The rejection ratios are significantly reduced from 40.8% and 30.6% of M0 membrane to 2.7% and 10.1% of M3 membrane, respectively. The negatively charged surface of PHI/PVDF membranes attract BR46 and MB dyes by the strong electrostatic interaction. Due to the limited aromatic ring system and weak π–π stacking interaction, BR46 and MB exhibit low hydrophobicity. This reduces their adsorption capacity onto the hydrophobic PVDF membrane, causing them to pass through the membrane easily and resulting in inefficient rejection. However, the rejection ratios of RhB and MG are basically unchanged with the increase in PHI addition (Fig. 10). The phenomenon can be ascribed to the strong interactions between RhB/MG and PVDF membrane, which are facilitated by their larger aromatic ring system, robust π–π stacking interaction, and enhanced hydrophobicity. RhB and MG are drawn to the membrane surface through electrostatic interaction, and are firmly adsorbed at the adsorption sites, making them difficult to desorb. Due to adsorption saturation, the adsorption amount is independent of the surface potential. Therefore, the rejection performances of cationic dyes with strong hydrophobicity and adsorption capacity are basically unchanged, which is not closely related to the surface charge. However, the rejection performances of cationic dyes with poor hydrophobicity and weak adsorption capacity decrease as the negative surface charge of PHI/PVDF membranes increases. For anionic dyes, the rejection ratios increase with molecular weight (CR (696.6 g mol^{-1}) > OG (452.3 g mol^{-1}) > MO (327.3 g mol^{-1})). Therefore, the molecular sieve effect works for the rejection of anionic dyes with different molecular weight. The rejection performance for MO with smaller molecular weight is gradually increased from 22.0% of M0 membrane to 62.5% of M3 membrane. The reason is attributed to the increased negative charges in the PHI/PVDF membranes with the PHI addition. The negatively charged surface of PHI/PVDF membranes effectively repulses the negatively charged MO dye. The greater the surface charge, the stronger the repulsion effect, and the higher the rejection rate. The rejection performance of OG and CR with larger molecular weight is not obviously affected by the PHI addition. The reason may be that the molecular weight of CR and OG is large enough to be effectively rejected by the membrane pores on the top surface. The surface charge has little effect on the rejection performance. Therefore, the molecular sieve effect mainly works for the rejection of anionic dyes with larger molecular weight. And Donnan effect plays the decisive role in the rejection of anionic dyes with small molecular weight.

The rejection performance of M1 membrane for different mixed dyes is further studied in detail. As shown in Fig. 11(a–c), once cationic dyes (MB, MG, BR46) mixes with anionic CR dye, the rejection ratios of MB, MG and BR46 are significantly improved. About 99.3% of MB, 91.8% of MG and 95.9% of BR46 is rejected (Table S3†). The reason may be owing to the electrostatic interaction of sulfonic acid groups in CR and cationic groups in cationic dyes, causing to the formation of micron-sized aggregates. The aggregates can't pass through the membrane pores and thus increasing the rejection ratio of cationic dyes.[60] Similar results are obtained by the M0 membrane for the rejection of different mixed dyes (Fig. S10 and Table S3†). However, for the cationic RhB dye, the rejection ratio only increases from 10.7% to 31.8% (Fig. 11(d) and Table S3†). The reason may be owing to the presence of carboxylic group in RhB structure (Table S1†), which hinders the sulfonic acid groups in CR to interact with the quaternary ammonium groups in RhB to form aggregates.[59] To further prove these conclusions, different cationic dyes (MB, MG, BR46 and RhB) are mixed with anionic MO dye. As shown in Fig. S11 and S12,† M1 and M0 membranes show the similar rejection performances for mixed dyes with MO. Therefore, prepared membranes can exhibit excellent rejection performance for most dyes in the treatment of mixed anionic and cationic dye solution.

Table 1 compares the dye rejection performance of M1 membrane with other separation membranes. It can be seen that M1 membrane prepared in our work has the comparable

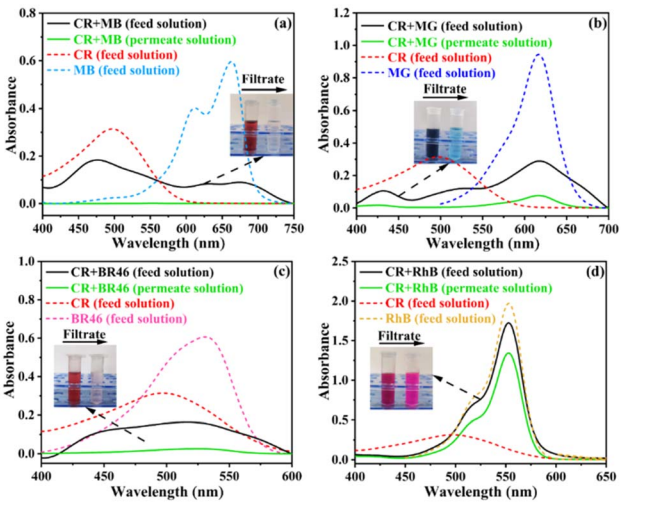

Fig. 11 The rejection performance of M1 membrane for different mixed dyes: (a) CR + MB, (b) CR + MG, (c) CR + BR46, (d) CR + RhB.

Table 1 Comparison of the water flux and dye rejection performance between M1 membrane and other separation membranes

Membrane	Flux (L m^{-2} h^{-1} bar^{-1})	Dye	Rejection ratio (%)	Reference
PES/SPSf TUF membrane	72.20	Methyl orange	62.4	17
1 wt% GO-PVA-NaAlg/PVDF	27.43	Methyl orange	93.6	18
		Congo red	95.9	
PoPD-PVA/Pz-MP	37.28	Congo red	99.7	61
TiO_2@ZIF-67/PVDF	130.70	Congo red	95.7	62
PIL-TiO_2/PSf	26.3	Methyl orange	30.9	63
		Congo red	94.2	
PVDF/PDA-TiO_2 (M-180)	226.70	Congo red	98.7	64
PHI/PVDF (M1)	361.31	Methyl orange	50.3	This work
		Congo red	99.8	

dye rejection performance. More importantly, the pure water flux of M1 membrane is much higher than those reported in other work, implying that M1 membrane can have high efficiency in treating dye solution.

To explore the consecutive stability and processing capacity of PHI/PVDF membrane on dye solution, the separation performance of M1 membrane for 50 mg per L CR solution is tested for a period of time. The result is shown in Fig. 12. It can be seen that the flux of CR solution decreases rapidly within the first 50 min, which is ascribed to the massive accumulation of CR molecules on membrane surface (Fig. S13†). After that, due to the electrostatic repulsion, CR molecules are difficult to continue accumulating on the membrane surface, resulting in a slow decrease in flux. After 120 min of operation, the flux still remains at 213.60 L m^{-2} h^{-1} bar^{-1} and about 613 L m^{-2} of CR solution has been processed. Meanwhile, the rejection ratio of CR remains basically stable, with always above 98%. In contrast, the flux of M0 membrane declines rapidly to 153.4 L m^{-2} h^{-1} bar^{-1} and only 500 L m^{-2} of CR solution is treated, although the rejection rate of CR keeps at above 98% (Fig. S14†). This result demonstrates that the PHI/PVDF membrane can achieve highly efficient rejection performance for CR dye in a long time and simultaneously possesses high water flux.

3.2.4. Self-cleaning performance and mechanism. Due to the accumulation of dye molecules on the membrane surface leading to the decrease in flux, it is necessary to adopt an effective method to remove the accumulated dye molecules. As can be seen from Fig. 13(a), under simulated sunlight irradiation, the color of M1 membrane polluted by CR dye gradually fades in the presence of H_2O_2. After 60 min of reaction, almost CR dye has been removed. However, in the absence of single light irradiation (Fig. 13(b)) or H_2O_2 (Fig. 13(c)), the color of polluted M1 membrane has no obvious change after 120 min. Therefore, light irradiation and H_2O_2 are indispensable. In addition, the self-cleaning performance of M0 membrane is also evaluated under the same conditions (light and H_2O_2). It can be seen from Fig. 13(d) that the color of polluted M0 membrane is basically unchanged. It can be thus concluded that the presence of PHI in M1 membrane can effectively remove organic pollutants from the polluted membrane under the light irradiation with the assistant of H_2O_2, thereby endowing PVDF membranes with excellent self-cleaning performance. However, when 0.5 g PHI is introduced, the color of M0.5 membrane is slightly faded after treatment of 120 min. Massive CR molecules still remain on the membrane (Fig. S15(a)†). This result implies that 0.5 g of PHI is not enough. When PHI addition is 2 g and 3 g, almost CR molecules can also be removed after 120 min (Fig. S15(b and c)†). The self-cleaning effect of M2 and M3 membranes is not further enhanced compared to that of M1 membrane. The reason may be caused by the agglomeration of excess PHI (Fig. 4(D-c and E-c)), which impedes PHI to function effectively.

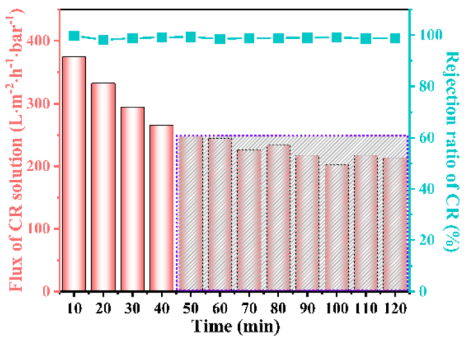

Fig. 12 The durability of M1 membrane on the treatment of CR solution.

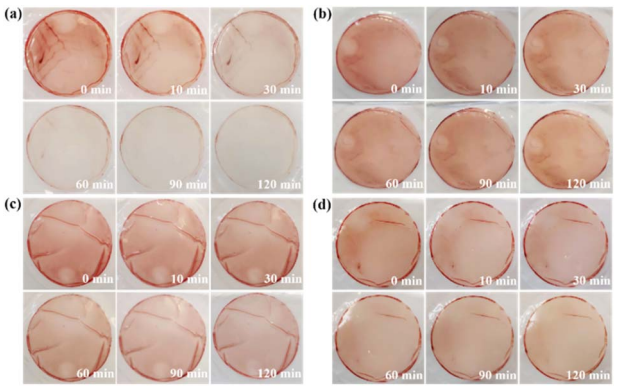

Fig. 13 Photographs of the color changes of polluted (a–c) M1 membrane and (d) M0 membrane with reaction time under different conditions: (a) light and H_2O_2, (b) H_2O_2, (c) light, (d) light and H_2O_2.

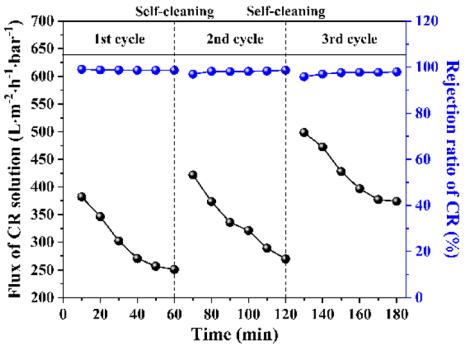

Fig. 14 Stability and rejection performance of M1 membrane at different cycles of self-cleaning treatment.

To further assess the effect of self-cleaning on the stability and rejection performance of PHI/PVDF membranes, cyclic experiment is conducted. The M1 membrane initially rejects the CR solution for 60 min, and then self-cleaned for 60 min in the presence of H_2O_2 and light irradiation. Subsequently, the M1 membrane is used for the next cycle. It can be seen from Fig. 14 that the rejection ratio of CR is only slightly reduced after the self-cleaning treatment. However, above 95.8% of CR can still be rejected after two cycles. In addition, the CR flux of M1 membrane increases slightly after the self-cleaning treatment, which may be due to the influence of the oxidative environment created by the excitation of PHI under light irradiation and with H_2O_2 on the membrane structure.

To clarify the mechanism of PHI/PVDF membranes in removing dye molecules under H_2O_2 and light irradiation, a series of trapping experiments for free radicals are conducted to identify the primary reactive species. As shown in Fig. 15, in the presence of methanol (MeOH) and chloroform (CF), the catalytic performance is slightly inhibited, indicating that $^{\bullet}OH$ and $^{\bullet}O_2^-$ are participated in the catalytic reaction, but not the main reactive species. Once triethanolamine (TEOA) is added into the reaction system, the catalytic performance is obviously suppressed, implying that h^+ plays the critical role in reaction. When $KBrO_3$ is introduced, the catalytic performance is significantly enhanced. The reason may be due to the capture of e^- by $KBrO_3$,[65] promoting the separation efficiency of photogenerated carriers, and thus leading to the generation of

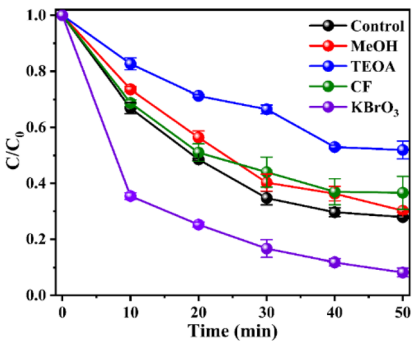

Fig. 15 Effects of different scavengers on the catalytic degradation of CR by PHI. Experimental conditions: [PHI] = 1 g L^{-1}, [H_2O_2] = 80 mM, [CR] = 20 mg L^{-1}, T = 30 °C.

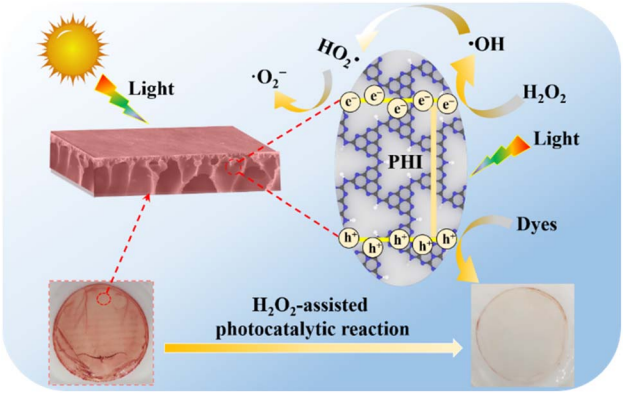

Fig. 16 Proposed self-cleaning mechanism for the removal of CR dye on PHI/PVDF membrane.

massive h^+ to degrade CR dye. This result further proves the positive role of h^+ in the catalytic reaction.

Based on the above experimental results, a possible self-cleaning mechanism for the removal of organic pollution on PHI/PVDF membranes is proposed. As shown in Fig. 16, PHI as a semiconductor photocatalyst in the membrane can adsorb the light energy greater than the bandgap energy and then is excited to produce photogenerated holes and electrons under simulated sunlight irradiation (eqn (8)). The produced photogenerated electrons are captured by H_2O_2 (HO–OH), leading to the broken of peroxide bond (–O–O–) in H_2O_2. One part of H_2O_2 is converted into hydroxyl radicals ($^{\bullet}OH$), while the other part gained the electrons is converted into hydroxide ions (OH^-) (eqn (9)).[66] Simultaneously, the consumed photogenerated electrons suppresses the recombination of photogenerated carriers. Otherwise, the produced photogenerated carries will recombine quickly and fail to act its role. Therefore, the remained photogenerated holes with high oxidation ability directly decompose the organic pollutants on the membrane surface. In addition, the formed $^{\bullet}OH$ can react with H_2O_2 to produce $HO_2^{\bullet}$, and which is further decomposed to $^{\bullet}O_2^-$ (eqn (10) and (11)).[67] The generated $^{\bullet}OH$ and $^{\bullet}O_2^-$ also participate in the degradation of organic pollutants. Therefore, PHI is excited under light irradiation, enabling it to work synergistically with H_2O_2 to generate various reactive species. These reactive species effectively decompose organic pollutants, thereby endowing the PHI/PVDF membranes with excellent self-cleaning capability.

$$PHI + h\nu \rightarrow h^+ + e^- \quad (8)$$

$$e^- + H_2O_2 \rightarrow {}^{\bullet}OH + OH^- \quad (9)$$

$$^{\bullet}OH + H_2O_2 \rightarrow H_2O + HO_2^{\bullet} \quad (10)$$

$$HO_2^{\bullet} \rightarrow H^+ + {}^{\bullet}O_2^- \quad (11)$$

4 Conclusions

In this work, efficient anti-fouling and self-cleaning PHI/PVDF membranes are successfully synthesized by the NIPS method for the rejection of BSA and high-flux dye removal. The

introduction of PHI, especially for M1 membrane, not only doesn't affect the rejection performance of BSA (≥97%), but also significantly enhances the mechanical property, water permeability and anti-fouling performance. The pure water flux and flux recovery ratio of M1 membrane are 361.31 L m^{-2} h^{-1} bar^{-1} and 89.97%, respectively, which is increased by 41.56% and 24.85% compared to the pure PVDF membrane. In addition, M1 membrane shows high rejection performance for anionic dyes, in which Donnan effect plays the critical role, especially for those of low molecular weight. Furthermore, the rejection ratio increases with the molecular weight, which is attributed the molecular sieving effect. 99.8% of CR dye can be rejected. Within 2 h of operation, about 613 L m^{-2} of 50 mg per L CR solution is processed with no decrease in rejection ratio (>98%). In the presence of anionic dye, the rejection performances for cationic dyes are significantly improved, which is due to the formation of micron-sized aggregates between cationic dye and anionic dye. And the accumulated dyes on M1 membrane surface can be easily removed within 60 min by the H_2O_2-assisted photocatalytic reaction, endowing it with efficient self-cleaning performance. And photogenerated h^+ is proved to be the main reactive species responsible for the self-cleaning function. Overall, the prepared PHI/PVDF membranes demonstrate considerable promise in the separation of BSA and the treatment of dyeing wastewater.

Data availability

The data supporting this article are provided as part of the ESI.† Raw experimental data are available from the corresponding author on reasonable request.

Conflicts of interest

There are no conflicts to declare.

Acknowledgements

This work was supported by the National Natural Science Foundation of China (52200129) and the Natural Science Foundation of Shandong Province of China (ZR2024ME158 and ZR2022QE130).

References

1 X. Zheng, Z. Zhang, D. Yu, X. Chen, R. Cheng, S. Min, J. Wang, Q. Xiao and J. Wang, *Resour., Conserv. Recycl.*, 2015, **105**, 1–10.
2 S. Samsami, M. Mohamadi, M. H. Sarrafzadeh, E. R. Rene and M. Firoozbahr, *Process Saf. Environ. Prot.*, 2020, **143**, 138–163.
3 Y. T. Lv, Y. Li, Y. Wang, X. Chen, R. Miao, X. Wang, C. Feng and L. Wang, *J. Water Process Eng.*, 2024, **59**, 105064.
4 U. Baig, M. Faizan and M. Sajid, *Adv. Colloid Interface Sci.*, 2020, **285**, 102276.
5 L. Ren, R. Deng, J. Yang, J. Li, J. Jin and T. Lei, *J. Mater. Sci.*, 2023, **58**, 13854–13864.
6 W. Ma, W. Ren, X. Bai, J. Pan, L. Huang, Q. Huang, Z. Guo and X. Wang, *J. Water Process Eng.*, 2022, **45**, 102504.
7 T. A. Otitoju, A. L. Ahmad and B. S. Ooi, *J. Water Process Eng.*, 2016, **14**, 41–59.
8 C. Kahrs and J. Schwellenbach, *Polymer*, 2020, **186**, 122071.
9 Z. Yang, Q. Liu, Q. Zhang, Y. Shen, Y. Shi, Y. Sun, Y. Li, Y. Peng and Q. F. An, *Sep. Purif. Technol.*, 2024, **341**, 126886.
10 E. Gadallah, J. C. Chen, M. N. Khalil, S. Karam and F. Li, *J. Water Process Eng.*, 2024, **63**, 105438.
11 Q. Liu, L. Li, X. Jin, C. Wang and T. Wang, *J. Mater. Sci.*, 2018, **53**, 6505–6518.
12 A. Aouni, C. Fersi, B. Cuartas-Uribe, A. Bes-Pía, M. I. Alcaina-Miranda and M. J. D. Dhahbi, *Desalination*, 2012, **297**, 87–96.
13 T. Lan, J. R. Song, Y. Chang and J. M. Xu, *J. Membr. Sci.*, 2025, **713**, 123318.
14 R. Ben Dassi, B. Chamam, J. P. Méricq, C. Faur, L. El Mir, I. Trabelsi and M. Heran, *Int. J. Environ. Sci. Technol.*, 2021, **18**, 2793–2804.
15 H. Nawaz, M. Umar, I. Nawaz, A. Ullah, M. Tauseef Khawar, M. Nikiel, H. Razzaq, M. Siddiq and X. Liu, *Adv. Eng. Mater.*, 2022, **24**, 2100719.
16 W. S. Chen, J. H. Mo, X. Du, Z. E. Zhang and W. X. Zhang, *Water Res.*, 2019, **151**, 243–251.
17 M. Y. Hu, S. Q. Yang, X. W. Liu, R. Tao, Z. Y. Cui, C. Matindi, W. Shi, R. Chu, X. Ma, K. Fang, M. Titus, B. B. Mamba and J. Li, *Sep. Purif. Technol.*, 2021, **266**, 118587.
18 A. Moghadam and A. Hemmati, *Sci. Rep.*, 2023, **13**, 8076.
19 S. Shen, Y. Shen, Y. Wu, H. Li, C. Sun, G. Zhang and Y. Guo, *Chem. Eng. Sci.*, 2022, **260**, 117934.
20 Y. Wang, Q. Li, T. Shao, W. Miao, C. You and Z. Wang, *Appl. Surf. Sci.*, 2022, **600**, 154133.
21 C. Ding, X. Qin, Y. Tian and B. Cheng, *J. Membr. Sci.*, 2022, **659**, 120789.
22 S. Xiang, X. Tang, S. Rajabzadeh, P. Zhang, Z. Cui and H. Matsuyama, *Sep. Purif. Technol.*, 2022, **301**, 122031.
23 J. Zhang, Y. Yang, Z. Sun, D. Zhao, Y. Gao, T. Shen, Y. Li, Z. Xie, Y. Huo and H. Li, *J. Membr. Sci.*, 2023, **677**, 121611.
24 X. Wei, S. Naraginti, X. Yang, X. Xu, S. P. Sun, R. Maligal-Ganesh, K. Sathishkumar and P. Chen, *Chem. Eng. J.*, 2024, **497**, 154718.
25 W. Wang, X. Fan, Z. Shu, J. Zhou and D. Meng, *Carbon*, 2023, **205**, 76–85.
26 W. Ma, J. Pan, W. Ren, L. Chen, L. Huang, S. Xu and Z. Jiang, *J. Membr. Sci.*, 2022, **659**, 120792.
27 S. Yang, X. Deng, P. Chen, T. Zhao, F. Liu, C. Deng and S. F. Yin, *Appl. Catal., B*, 2022, **311**, 121370.
28 A. Ghaffar, L. Zhang, X. Zhu and B. Chen, *Environ. Sci. Technol.*, 2018, **52**, 4265–4274.
29 Z. Zhao, J. Zhou and Z. Shu, *Chem. Eng. J.*, 2022, **449**, 137868.
30 W. Wang, Z. Shu, Z. Liao, J. Zhou, D. Meng, T. Li, Z. Zhao and L. Xu, *Chem. Eng. J.*, 2021, **424**, 130332.
31 G. Zhang, Y. Xu, C. He, P. Zhang and H. Mi, *Appl. Catal., B*, 2021, **283**, 119636.
32 W. Wang, Z. Shu, J. Zhou, D. Meng, Z. Zhao and T. Li, *J. Mater. Chem. A*, 2020, **8**, 6785–6794.
33 W. Wang, Z. Shu, J. Zhou and D. Meng, *Sep. Purif. Technol.*, 2023, **318**, 124027.

34 Z. Zhao, Z. Shu, J. Zhou, L. Ye, T. Li, W. Wang and L. Xu, *J. Mater. Chem. A*, 2022, **10**, 17668–17679.
35 M. Zhou, L. Zeng, R. Li, C. Yang, X. Qin, W. Ho and X. Wang, *Appl. Catal., B*, 2022, **317**, 121719.
36 B. Li, B. Wang, Z. Liu and G. Qing, *J. Membr. Sci.*, 2016, **517**, 111–120.
37 K. Valizadeh, A. Heydarinasab, S. S. Hosseini and S. Bazgir, *J. Ind. Eng. Chem.*, 2022, **106**, 411–428.
38 X. Yue, X. Ji, H. Xu, B. Yang, M. Wang and Y. Yang, *Energy*, 2023, **273**, 127215.
39 M. Chen, N. Hu, W. Wang, L. Lei, H. Fan, P. Müller-Buschbaum and Q. Zhong, *Adv. Funct. Mater.*, 2024, **34**, 2402477.
40 C. Geng, L. A. Fan, H. Niu, L. Liu, F. Zhao, J. Zhang, H. Dong and S. Yu, *Mat. Sci. Eng. C*, 2021, **131**, 112517.
41 A. Abdel-Karim, J. M. Luque-Alled, S. Leaper, M. Alberto, X. Fan, A. Vijayaraghavan, T. A. Gad-Allah, A. S. El-Kalliny, G. Szekely, S. I. A. Ahmed, S. M. Holmes and P. Gorgojo, *Desalination*, 2019, **452**, 196–207.
42 C. Li, T. Sun, G. Yi, D. Zhang, Y. Zhang, X. Lin, J. Liu, Z. Shi and Q. Lin, *J. Environ. Chem. Eng.*, 2022, **10**, 108488.
43 C. Ma, J. Hu, W. Sun, Z. Ma, W. Yang, L. Wang, Z. Ran, B. Zhao, Z. Zhang and H. Zhang, *Chemosphere*, 2020, **253**, 126649.
44 Z. Liang, J. Wang, Q. Zhang, T. Zhuang, C. Zhao, Y. Fu, Y. Zhang and F. Yang, *Sep. Purif. Technol.*, 2021, **276**, 119308.
45 E. Abdollahi, A. Heidari, T. Mohammadi, A. A. Asadi and M. A. Tofighy, *Sep. Purif. Technol.*, 2021, **257**, 117931.
46 R. Y. Chang, R. Li, W. Wang, W. H. Geng, N. Li, L. C. Jing, Z. X. Yang, J. Li and H. Z. Geng, *J. Membr. Sci.*, 2024, **693**, 122360.
47 A. Karimi, A. Khataee, A. Ghadimi and V. Vatanpour, *J. Environ. Chem. Eng.*, 2021, **9**, 105115.
48 N. G. P. Chew, S. Zhao, C. Malde and R. Wang, *J. Membr. Sci.*, 2018, **563**, 31–42.
49 V. Vatanpour, M. Esmaeili, S. Chahvari and M. Masteri-Farahani, *J. Environ. Chem. Eng.*, 2021, **9**, 105900.
50 M. S. A. Saraswathi, D. Rana, N. J. Kaleekkal, K. Divya and A. Nagendran, *J. Environ. Chem. Eng.*, 2020, **8**, 104426.
51 H. Yu, L. Gu, S. Wu, G. Dong, X. Qiao, K. Zhang, X. Lu, H. Wen and D. Zhang, *Sep. Purif. Technol.*, 2020, **247**, 116889.
52 C. Li, X. Chen, J. Luo, F. Wang, G. Liu, H. Zhu and Y. Guo, *Sep. Purif. Technol.*, 2021, **259**, 118127.
53 P. Li, H. Liang, X. Luo, X. Cheng, J. Ding, D. Wu, L. Liu, X. Gao and G. Li, *J. Membr. Sci.*, 2022, **662**, 120984.
54 D. D. Kachhadiya and Z. V. P. Murthy, *J. Membr. Sci.*, 2023, **676**, 121607.
55 W. Wang, X. Xu, Z. Zhang, P. Zhang, Y. Shi and P. Ding, *Colloid Interface Sci. Commun.*, 2021, **43**, 100433.
56 C. Yang, Z. Zhang, P. Wang, P. Xu, T. Shen, M. Wang, Q. Zheng and G. Zhang, *J. Hazard. Mater.*, 2023, **451**, 131154.
57 G. Palanisamy, H. O. Mohamed, P. D. Kolubah, Y. M. Im, S. Thangarasu, A. R. Hari, P. E. Saikaly, P. Castaño and T. H. Oh, *Chem. Eng. J.*, 2024, **497**, 154597.
58 J. Zhu, S. Zhou, M. Li, A. Xue, Y. Zhao, W. Peng and W. Xing, *J. Membr. Sci.*, 2020, **612**, 118467.
59 T. T. Van Tran, S. R. Kumar and S. J. Lue, *J. Membr. Sci.*, 2019, **575**, 38–49.
60 J. Wu, J. Liu, B. Wen, Y. Li, B. Zhou, Z. Wang, S. Yang and R. Zhao, *Chemosphere*, 2021, **272**, 129622.
61 D. Beqqour, W. Taanaoui, G. Derouich, M. Ouammou, S. A. Younssi, J. Bennazha and J. A. Cody, *Desalin. Water Treat.*, 2022, **257**, 23–33.
62 N. Prabhakar, A. M. Isloor, M. Padaki and A. F. Ismail, *Chem. Eng. J.*, 2024, **498**, 155270.
63 U. Nellur, K. S. Kavya, N. S. Naik and M. Padaki, *J. Cleaner Prod.*, 2024, **483**, 144268.
64 Y. Y. Shi, X. Chen, Q. Q. Wu, H. Z. Zhen, S. Wang, H. L. Dong, J. Z. Wang and Y. Li, *J. Environ. Chem. Eng.*, 2023, **11**, 110389.
65 R. Sharma, V. Kumar, S. Bansal and S. Singhal, *J. Mol. Catal. A:Chem.*, 2015, **402**, 53–63.
66 Y. Wang, H. Song, J. Chen, S. Chai, L. Shi, C. Chen, Y. Wang and C. He, *Appl. Surf. Sci.*, 2020, **512**, 145650.
67 C. Yu, R. Huang, Y. Xie, Y. Wang, Y. Cong, L. Chen, L. Feng, Q. Du, W. Sun and H. Sun, *Sep. Purif. Technol.*, 2022, **295**, 121334.